Advanced Functional Materials

ADVANCED FUNCTIONAL MATERIALS
www.afm-journal.de

RESEARCH ARTICLE OPEN ACCESS

Multifunctional Gold Nanocluster-Based PROTAC System for Targeted Degradation of Phosphorylated Tau and Modulation of Neuroinflammation in Alzheimer's Disease

Sarah Nevins | Callan D. McLoughlin | Wan-Kyu Ko | Hye Kyu Choi | Brandon Conklin | Joshua B. Stein | Yannan Hou | Hongwon Kim | Rohan Khulbe | Ki-Bum Lee

Department of Chemistry and Chemical Biology, Rutgers, The State University of New Jersey, Piscataway, New Jersey, USA

Correspondence: Ki-Bum Lee (kblee@rutgers.edu)

Received: 4 December 2025 | **Revised:** 28 April 2026 | **Accepted:** 21 May 2026

Keywords: gold nanoclusters (AuNCs) | neurodegenerative diseases | neuroinflammation | proteolysis-targeting chimera (PROTAC) | reactive oxygen species (ROS) Scavenging

ABSTRACT

Alzheimer's disease (AD) is the most prevalent neurodegenerative disorder and lacks treatments capable of significantly altering disease progression or patient outcomes. Consequently, novel therapeutic strategies targeting key pathological features such as phosphorylated tau (pTau) aggregation and chronic inflammation are urgently needed. In this work, we present a novel proteolysis-targeting chimera (PROTAC) system conjugated to lipoic acid gold nanoclusters (PLANC), designed to degrade pTau, regulate inflammatory signaling, and effectively traverse the blood-brain barrier (BBB). PLANC demonstrated the ability to significantly degrade pTau at various phosphorylation sites, with mechanistic studies confirming proteasome-mediated degradation via cereblon recruitment. Moreover, PLANC effectively scavenged reactive oxygen species (ROS) and modulated NF-κB and mTOR pathways in human astrocytes and mature neurons, further highlighting its anti-inflammatory capabilities. We demonstrated that PLANC successfully traversed the BBB using a physiologically relevant transwell model composed of astrocytes and endothelial cells with confirmed tight junction formation. Finally, the addition of pTau-induced neurons created a BBB model to better represent changes in the AD environment. Collectively, these findings position PLANC as a robust and multifunctional therapeutic platform capable of simultaneously targeting the multifaceted pathologies of AD, including pTau aggregation, neuroinflammation, and oxidative stress.

1 | Introduction

Neurodegenerative diseases (NDs), such as Alzheimer's disease (AD) and Parkinson's disease (PD), are characterized by the progressive loss of neuronal structure and function, which ultimately leads to neuronal death. Therapeutic development for NDs is hindered by numerous challenges, including the delivery of drugs across the blood-brain barrier (BBB), and the effective targeting of complex pathological entities, such as protein aggregates, misfolded proteins, and inflammatory mediators. For example, AD is defined by hallmark pathological features, including amyloid-beta plaques, neurofibrillary tangles, and chronic neuroinflammation. Despite being the most prevalent neurodegenerative disease, treatments capable of halting or reversing AD progression are lacking [1–6]. To this end, neurofibrillary tangles (NFTs), composed of tau protein aggregates, have become important therapeutic targets because of their crucial connection to neuron degeneration and cell death [7–9]. As AD progresses, Braak staging is used to define tau spreading throughout the brain [10]. Cell-to-cell spreading of tau leads to the expression of

pathological tau in multiple cell types and to the amplification of pTau expression in the neocortex with the sensory, motor, and visual cortexes coming last. Moreover, recent studies have revealed a strong link between oxidative stress and excessive tau phosphorylation. Excessive pTau formation is known to impair mitochondrial function, although the underlying mechanisms warrant further investigation [2, 11]. Inflammation has also been identified as a critical factor in AD, closely tied to both tau phosphorylation and oxidative stress [12]. Elevated NADPH oxidase (NOX) activity and the resulting reactive oxygen species (ROS) production increase inflammatory cytokine expression and NF-κB signaling [13]. Among NOX subunits, NOX4 is specifically implicated in tauopathy development and upregulated in AD [14]. Conventional small-molecule inhibitors and drug delivery systems have had limited success in addressing the intricate and interrelated pathologies of tau aggregation, inflammation, and oxidative stress. This insufficiency underscores a pressing need for innovative therapeutic strategies and approaches to overcome these challenges and improve treatment outcomes.

Given the interconnected and multifactorial nature of AD pathology, single-target therapies are unlikely to yield significant success. Therefore, developing a multifaceted therapeutic strategy capable of simultaneously targeting multiple disease-driving processes would be imperative. Targeted protein degradation (TPD) technologies have emerged as an attractive alternative approach toward this goal. TPD has the potential to overcome these limitations by causing the degradation of disease-causing proteins, thereby eliminating their function entirely [15–17]. For instance, the proteolysis-targeting chimera (PROTAC) system utilizes the ubiquitin-proteasome pathway (UPP) to degrade proteins that are otherwise difficult to target directly [17]. PROTAC molecules are composed of a bifunctional structure, linking a ligand that binds an E3 ligase to another ligand that binds a protein of interest (POI). This approach has been successfully used to degrade various proteins with high specificity selectively [18–20]. Moreover, PROTACs have been engineered to enhance efficiency by incorporating them onto nanoparticles capable of degrading multiple proteins simultaneously, thereby improving therapeutic outcomes [21]. Current PROTAC systems, including nanoparticle-based approaches, have primarily focused on cancer applications. Although some small-molecule and peptide PROTACs have been used for AD and other neurodegenerative conditions, there have been no demonstrations, to our knowledge, of both BBB penetration and simultaneous targeting of inflammatory pathways like NF-κB and Casp3 for neuroprotection [22–24]. While PROTAC shows promise for treating neurodegenerative diseases [25], significant challenges include limited cellular uptake, poor BBB penetration, and low aqueous solubility, resulting in inadequate bioavailability.

Gold nanoclusters (AuNCs), characterized by their ultra-small size (<2 nm), have garnered increasing attention in the past two decades for their potential biomedical applications [26, 27]. The precise arrangement of gold atoms within the core lattice, combined with the surrounding uniform gold–sulfur network, allows for atomically precise structures [28–30]. Moreover, by optimizing ligand choice, gold-to-ligand ratios, and core size, researchers can finely tune the spacing and number of ligands per cluster [31, 32]. This precise control over surface chemistry, combined with an ultra-small size and efficient renal clearance, makes AuNCs highly suitable inorganic candidates for in vivo therapeutic development [33–36]. Lipoic acid (LA), a potent antioxidant with known anti-inflammatory properties, can be used as a capping agent for AuNCs, forming stable thiol–gold bonds [37–39]. Dihydrolipoic acid (DHLA), with its two thiol groups, enables AuNC capping with approximately half the number of surface ligands compared to monothiol ligands due to a disulfide bond. DHLA scavenges free radicals, is known to produce endogenous antioxidants like ascorbic acid, and chelates metal ions [40, 41]. Furthermore, LA can modulate the NF-κB activity, induced nitric oxide synthase (iNOS) levels, and NLRP3 inflammasome activation [42, 43]. In clinical trials of LA delivery, TNF-α and IL-6 levels have been shown to dramatically decrease [44]. Importantly, LA-capped AuNCs retain the inherent ROS scavenging and anti-inflammatory properties of LA and have showed neuroprotective effects by influencing mitochondrial metabolic function [38, 41, 43, 45]. LA AuNCs have also been well studied in vivo and led to no observed adverse effects [46–48].

To address the challenges described above, herein, we developed Proteolysis Targeting LA AuNCs (**PLANC**) as a novel therapeutic strategy for AD. Our platform is designed to degrade phosphorylated tau (pTau), scavenge ROS, and regulate pro-inflammatory factors. In addition to these benefits, PLANC's tunable nanometer dimensions point toward a promising ability to cross the BBB, which is essential for successfully treating neurodegenerative conditions. To construct PLANC, we conjugated poly(ethylene glycol) 1000 (PEG) to LA and either toluidine blue O (Tol blue) or pomalidomide (Pom) as PROTAC ligands through a series of syntheses [49]. Tol blue binds to pTau, while Pom targets cereblon, an E3 ubiquitin ligase. By incorporating these ligands into the AuNC synthesis, we aimed to create a multifunctional nanoparticle capable of degrading pTau and modulating inflammatory pathways. PLANC degrades pTau with the proteasome and retains the antioxidant and anti-inflammatory properties of LA AuNCs (Figure 1a,b). In summary, the developed PLANC system effectively integrates multiple therapeutic modalities: the inherent antioxidant and anti-inflammatory properties of LA AuNCs, coupled with targeted protein degradation capabilities for pTau. The demonstrated ability of the PLANC system to penetrate the BBB, as shown in our transwell studies, highlights its potential as a promising multifunctional therapeutic platform for addressing NDs (Figure 1c). By simultaneously addressing tau aggregation, oxidative stress, and neuroinflammation, this innovative nanoplatform represents a significant advance in developing more effective treatments for AD and potentially other neurodegenerative disorders characterized by protein aggregation and chronic inflammation.

2 | Results and Discussion

2.1 | Development of the PLANC Platform: Design, Synthesis, and Characterization of a Multifunctional Nanocarrier

In this work, we synthesize and demonstrate that PLANC is a novel multifunctional therapeutic system capable of simultaneously degrading pTau and regulating inflammation in neurons and astrocytes. This dual-action capability offers significant potential for the treatment of AD. The PLANC system was

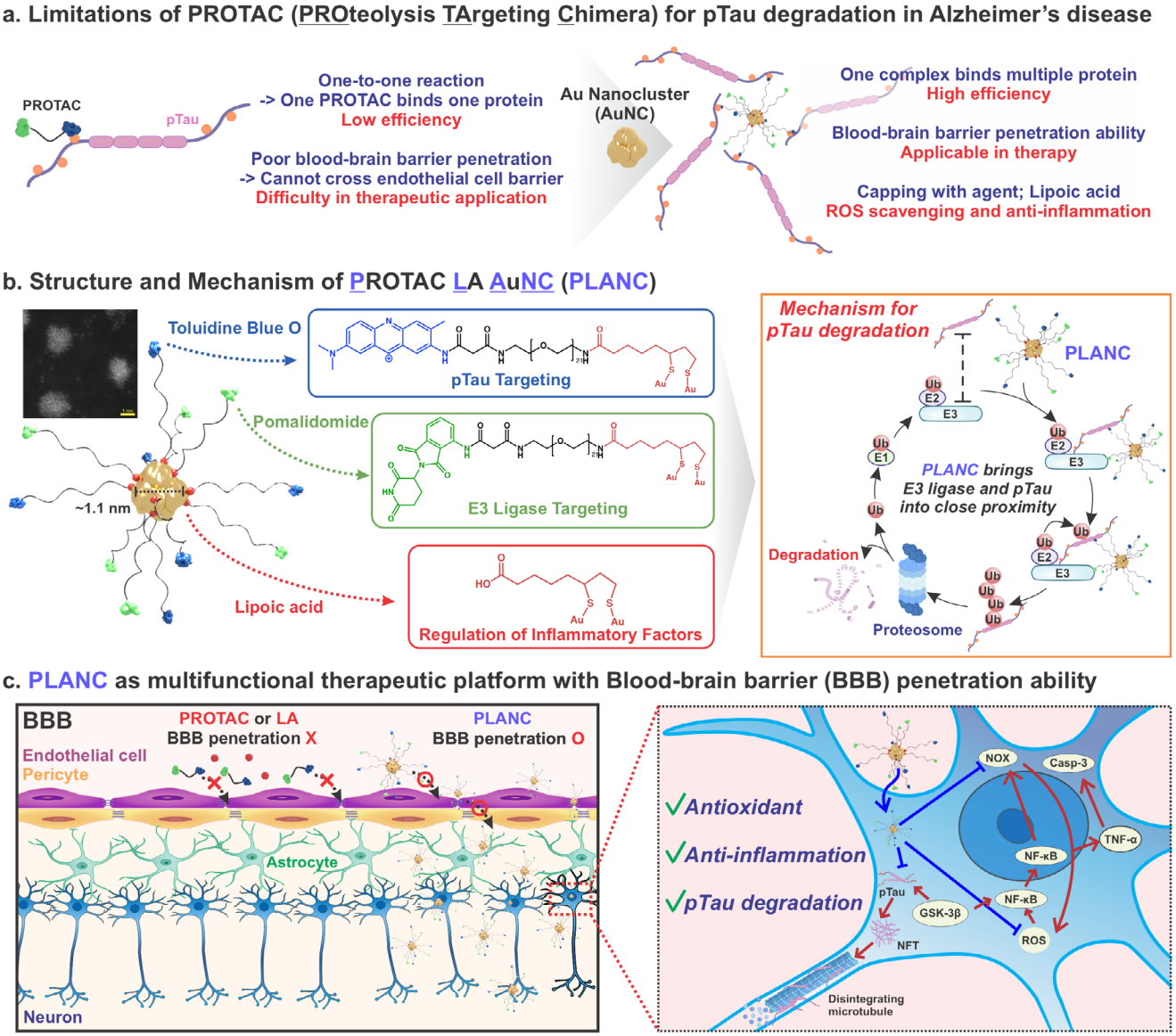

FIGURE 1 | Schematic of PLANC synthesis. (a) Comparison of potential small molecule PROTAC and LA co-delivery effects versus PLANC effects. (b) Structure of the ligands used for PLANC synthesis. Formation and Ultra-STEM imaging of PLANC. (c) Overview of the BBB and healthy environments, transwell model cell types, and immunostaining of Occludin and ZO-1 to confirm tight junction formation. Inset 1: PLANC scavenges ROS and regulates pro-inflammatory factors through interacting with NADPH oxidase. Inset 2: pTau is degraded by the proteasome due to PLANC delivery to cells.

synthesized through a multi-step process involving PEG modifications, conjugation of LA to PEG1000, and the subsequent formation of PLANC using established protocols for AuNC synthesis (Figure S1). For PLANC formation, LA-PEG-Pom and LA-PEG-Tol blue were put in a 1:1 ratio with varying combinations of spacer ligands, LA or LA-PEG, for an optimal distance between ligands for protein-small molecule binding (Figure 2a, Figures S2–S9). The degradation of pTau by the proteasome requires two distinct ligands during PLANC synthesis: LA-PEG-Tol blue, which binds to pTau, and LA-PEG-Pom, which binds to the cereblon E3 ligase [50–54]. As supported by prior studies, Tol blue targets pTau residues 14–16, while Pom interacts with cereblon [50–54]. LA plays a crucial role in PLANC formation, as the two sulfur atoms facilitate efficient binding to the AuNCs, effectively reducing the number of surface ligands required compared with monothiol ligands [55]. This controlled ligand density is critical for optimal PROTAC system function, as it ensures proper spacing and orientation of the small-molecule ligands on the AuNC surface [56]. As Tol blue specifically binds to pTau, replacing it with a different small molecule could allow the system to target other proteins associated with neurodegenerative diseases. This adaptability is particularly valuable, given the critical role of protein aggregation and inflammation in the pathology of many neurodegenerative disorders. This modular design positions PLANC as a versatile platform for developing targeted therapies beyond AD.

A PDB file was made of the relaxed structure of Tol Blue with molecular modeling, and Tol blue binding to stacked tau was simulated with Chimera, a well-known tool for small molecule

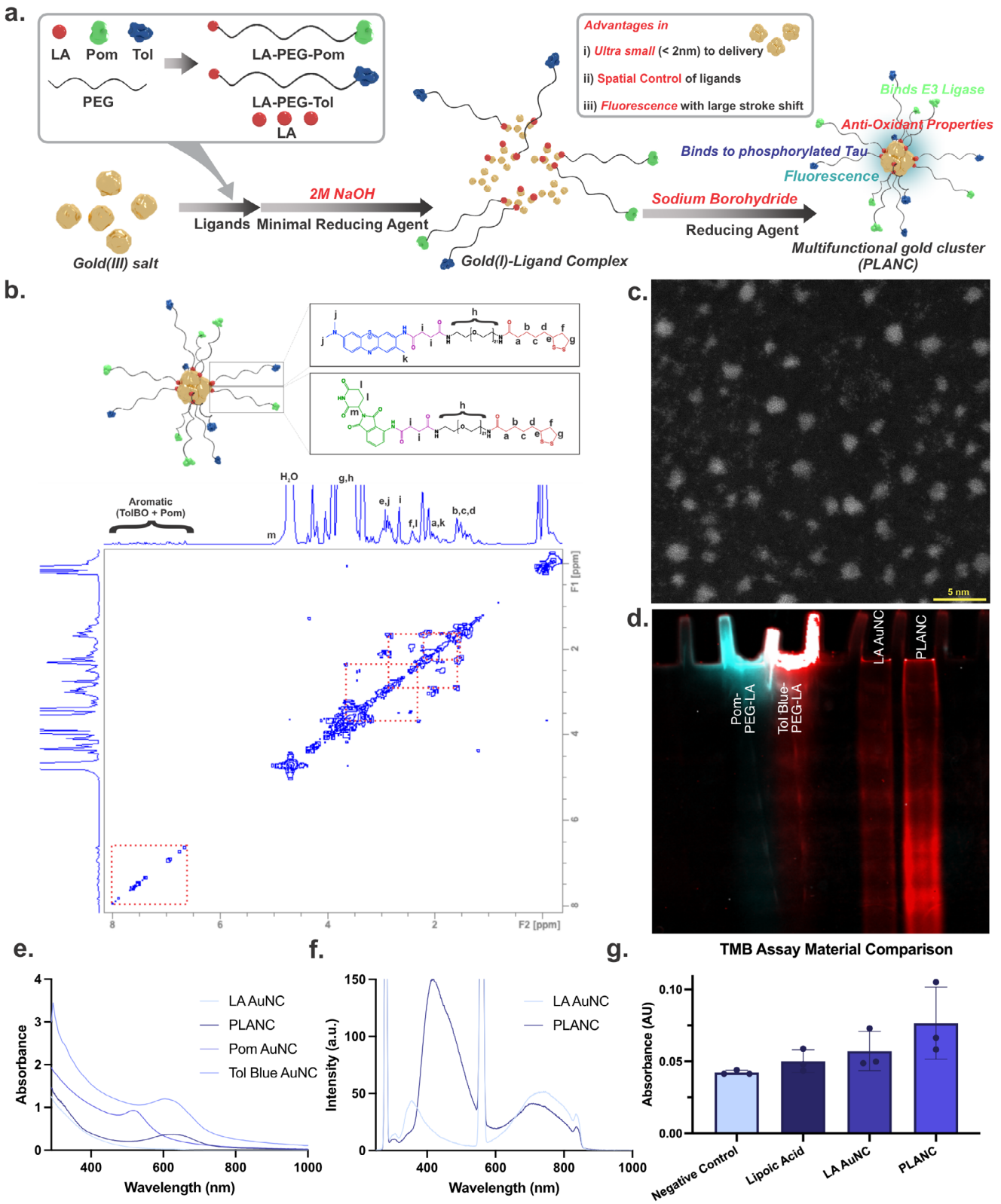

FIGURE 2 | (a) Schematic of PLANC synthesis. (b) ^{1}H-^{1}H COSY 2D NMR spectrum of PLANC with structures of the associated ligands. ^{1}H environments are labeled on the ligand structures and correspond with labels on the 1D projection. (c) Ultra-STEM image of PLANC core (scale bar = 5 nm). (d) overlayed fluorescence chanels for PLANC, Pomalidomide, and Toluidine Blue to visualize movement of clusters and ligands. (e) absorbance spectra of LA AuNC, Tol Blue-PEG-LA AuNCs, Pom-PEG-LA AuNC, and PLANC. (f) Fluorescence spectra of LA AuNC and PLANC. (g) TMB assay comparing the ROS scavenging activities of PROTAC LA AuNC, LA AuNC, and LA over time.

protein binding, to show potential states for binding to tau as well as where the binding interactions would occur (Figure S11). Chimera was then used to dock the small molecule as well as visualize and analyze potential interactions between Tol Blue and Tau. This binding event is crucial for pTau degradation, consistent with well-established literature reporting Tol Blue's affinity for pTau. However, modeling the potential binding to pTau computationally allows for further information about the potential interactions that could happen between the small molecule and protein as well as the theoretical binding sites. After choosing the ligand for pTau binding, ^{1}H NMR was used to confirm the formation of each step of ligand synthesis and PLANC formation (Figures S2–S9). Furthermore, the ratio of Pom: Tol Blue: LA on the surface of PLANC was determined to be 1:1.26:7.26 through relative quantification of the ligands with NMR (Figure S10). Therefore, 13.8% of ligands are LA-PEG-Pom, 17.4% of ligands are LA-PEG-Tol Blue, and 68.9% of ligands are LA alone. X-ray photoelectron spectroscopy (XPS) was used to confirm the elemental composition (Figures S12 and S13). Specifically, nitrogen is not present in the LA AuNC but is present in PLANC ligands for pTau and E3 ligase binding (Figure S12). PLANC has a zeta potential of −20.1 mV, which is not significantly different from the charge of LA AuNCs (Figure S14).

To gain a better understanding of the surface-state ligand chemistry at the interfaces of the LA AuNCs and PLANC, respectively, ^{1}H-^{1}H correlation spectroscopy (COSY) 2D NMR was conducted (Figure 2b; Figure S15). The ^{1}H NMR spectrum of PLANC collected previously (Figure S10) indicated that the ^{1}H resonances of the surface ligands were broadened, likely due to the chemical shift anisotropic effect. Additionally, complex splitting patterns were observed in the LA-PEG-Pom and LA-PEG-Tol blue ligands, especially for lipoic acid ^{1}H resonances. ^{1}H-^{1}H COSY NMR revealed a strong correlation between lipoic acid CH_2 groups (b,c,d) and the chiral CH group (e). Furthermore, we observed correlation between both CH_2 groups located adjacent to each other on the five-membered heterocycle (f and g). This indication was quite helpful, as the ^{1}H resonance for 'g' is buried beneath the dominating CH_2 signal attributed to the PEG ligand (h). Lastly, we observed some key aromatic ^{1}H resonances from both Pom and Tol blue, generally located from 6.5–8.0 ppm. Unfortunately, due to the diluted presence of Pom and Tol blue signals compared to that of lipoic acid and PEG signals, the non-aromatic CH_3 groups found on Tol blue (j and k) in addition to the CH and CH_2 groups found on Pom (l and m) are difficult to resolve. Despite this, ^{1}H-^{1}H COSY NMR revealed useful surface-state ligand chemistry for both LA-AuNCs and PLANC, providing a more comprehensive characterization technique for the developed system.

Transmission electron microscopy (TEM) and ultra-scanning transmission electron microscopy (STEM) were used to determine the size of the gold core averaged to 1.1 nm across multiple PLANC batches with gold core sizes ranging from about 0.7 to 1.4 nm (Figure 2c; Figure S16). STEM imaging further confirmed a lattice structure indicating AuNC formation. To better study the variation in the size of PLANC including the ligands, polyacrylamide gel electrophoresis (PAGE) was utilized. The differing fluorescence excitations and emissions of Pom-PEG-LA, Tol Blue-PEG-LA, and PLANC helped confirm AuNC formation as well, since neither ligand has a fluorescence with the same stoke shift as PLANC or LA AuNCs (Figure 2d; Figure S17a–c). Native PAGE results show a spread of sizes for the AuNCs with four main bands and a fifth lighter one, although the bands are not completely defined, likely due to some small variations in size due to the presence of PEG and the variety of ligands capping the surface (Figure 2d; Figure S17d). Furthermore, the free ligands could not move down the gel likely due to the size and fairly neutral charge. Therefore, a sodium dodecyl sulfate (SDS)-PAGE was run to additionally separate out the PEG ligands (Figure S17e). While the discrete bands of the LA AuNCs changed dramatically in the SDS-PAGE gel, likely due to interactions between SDS and the AuNCs, it did allow for better separation of the free PEG ligands. Notably, for PLANC, although the clusters bands became less discrete in the SDS-PAGE gel than in the native PAGE gel, the majority of PLANC came off with as a single intense broad band at a higher molecular weight than either of the free PEG molecules. While some of the PLANC sample migrated to the same location as the free ligand in the SDS-PAGE, the lack of free PEG in the native PAGE at the top of the well from the same sample suggests that is due to interactions with SDS, and not due to free ligand in solution with PLANC.

ESI-MS revealed two groups of peaks related to PLANC (Figure S18a). First, due to the purification of free ligands out from solution as well as the lack of free ligand in the native PAGE gel, LA-PEG-Tol Blue and LA-PEG-Pom peaks seen in the 400 – 800 m/z region appear to have dissociated from the complex during the ionization process (Figure S18b). Most of these ions showed +3 and +2 charge states with a deconvoluted average intact mass ranging between 1450 and 1620 Daltons. Second, high charge states of the intact PLANC clusters are evident in the m/z 1000–1800 ion region (Figure S18c). PLANC showed higher charges states distributions ranging from +20 to +15, however, there was not complete resolution between the isotopologues with respect to the intact molecule because of its conjugation to PEG. PEG usually dominates in the ESI-MS due to its intense signal that sometimes can mask or suppress the ions including the signal of the intact Au-LA cluster. A second reason for the resolution is that the complexity of the molecular design can make it a little challenging to vaporize into their gas phase. Finally, as PAGE gel electrophoresis showed there is a small range in sizes of PLANC. Therefore, each of these individual charge states becomes harder to resolve. The reasons for this range in sizes likely stem from LA as the choice in capping ligand. Due to the disulfide on the surface, AuNCs can potentially need only half the number of ligands for PLANC formation. For example, the $Au_{25}(SR)_{18}$ structure could potentially be achieved with $Au_{25}(LA)_9$ as there are still 18 thiols present to cap the AuNC during synthesis. Therefore, there is slightly more variation in the number of ligands on the surface. Although resolution was not perfect for the reasons discussed above, the m/z 1512.7601 ion showed a charge distribution around +16 (Figure S18d). Based on the ESI-MS data, the average intact molecular weight of PLANC came around 24439.3660 Daltons. Due to the lower signal intensity, smaller populations of PLANC showed molecular weight distributions from 17000–28000 Daltons. Although signal intensity generally correlates with the size of the population in ESI-MS, if vaporization to the gas phase is insufficient or if there is too high of a concentration, that can cause the signal intensity to not reflect the size of the population due to the extended dynamic range. Overall, as the AuNCs were shown to have some dispersity in atomic number through PAGE gel electrophoresis and ESI-MS,

there are likely a few populations of AuNCs such as Au25SR18, Au38SR26, Au42SR32, and Au52SR32 with varying numbers of LA to cap the surface due to the disulfide [57–59]. The percentage of each ligand capping the surface of PLANC is assumed to be similar to the proportion found among the whole population with ^{1}H-NMR based quantification of ligands in PLANC. As previously mentioned, the STEM data also correlates as there is a small distribution in the AuNC core size ranging from 0.7 to 1.4 nm. Due to the m/z found in ESI, the core size from STEM imaging, as well as the large molecular weight of the PEG ligands, it is unlikely that the largest AuNCs of the PLANC size distribution are much larger than 70 gold atoms. UV–vis spectra also indicated PLANC formation, Pom conjugation, and Tol blue conjugation to the AuNC surface (Figure 2e). By taking UV–vis of LA AuNCs as well as PLANC, the peaks specific to LA AuNCs versus PROTAC functionalized LA AuNCs can be determined. LA AuNCs as well as all other AuNC conditions had a small absorbance at 320 nm. Furthermore, UV–vis spectra for Pom-PEG-LA capped AuNCs is the only AuNC with a peak around 520 nm, and Tol Blue-PEG-LA capped AuNCs is the only AuNC with a peak around 630 nm. The final PLANC absorption spectra have a larger broad peak between these peaks due to the overlapping signals that peaks at about 590 nm. Furthermore, PLANC fluorescence spectra, when excited at 290 which led to a satellite peak at 580, showed emissions at 410 and 730 nm, while LA AuNCs showed a small emission at 360 as well as the emission at 740 nm (Figure 2f). The change in emissions is due to the intrinsic fluorescence of pomalidomide at 440 nm when excited at 290 nm. Combined, this data helped confirm PLANC formation with the preferred ligands. The stability of the nanoclusters was tested over time in several conditions including in media, H_2O_2, glutathione, and PBS by UV–vis and confirmed to consistently have a peak ranging from 550 to 650 nm in all conditions (Figure S19).

To investigate the ROS-scavenging activity of PLANC, we conducted a peroxidase-like activity assay using the 3,3′,5,5′-tetramethylbenzidine (TMB) method. Peroxidase-like activity catalyzes the formation of H_2O from H_2O_2 in acidic microenvironments, functionally scavenging the local peroxide. In general, TMB acts as an electron donor during localized peroxidase-like activity, shifting chromogenically from a colorless form to a blue form, known as a charge-transfer complex. For each H_2O_2 molecule that is catalyzed, one molecule of TMB is converted into its blue form, measurable by UV–vis spectroscopy. In this study, PLANC displayed higher peroxidase-like activity than LA and showed activity similar to LA AuNCs in a concentration-dependent manner (Figure 2g; Figure S20). The ROS scavenging, linked to peroxidase like activity, confirmed that both LA AuNCs and PLANC possessed better activity than LA alone. However, the antioxidant activity of LA through its disulfide bridge likely plays a role in the enhanced peroxidase-like activity of LA-AuNCs and PLANC, in combination with the known catalytic abilities of AuNCs.

2.2 | PLANC Optimization and Confirmation of Protein Degradation

SH-SY5Y, a human neuroblastoma cell line, is widely accepted as an in vitro model for the preliminary evaluation of potential AD therapeutics due to its ability to differentiate into neuron-like cells and express relevant AD-related proteins [60–62]. These cells, derived from human neural tissue, display neuron-like properties that make them particularly suitable for studying neurodegeneration and testing novel therapeutic approaches [60, 61]. Therefore, the cells were induced with okadaic acid (OA), a protein phosphatase 2A inhibitor, to cause excessive pTau and lead to downstream ROS formation [63–67]. We hypothesized that free LA on the AuNC surface would lead to increased protein degradation due to more space between ligands for protein binding. Therefore, pTau (S202/T205) degradation was compared with varying ratios of LA to LA-PEG-Pom and LA-PEG-Tol at the same concentration, and the best condition was determined to be a 3:1:1 ratio based on the quantification of pTau degradation (Figure S21). The additional space on the PLANC surface leading to better protein degradation shows that LA also likely increased the protein degradation, as PLANC was capped with half the number of ligands due to the disulfide versus other thiol-based ligands with a single sulfur. We then tested the ROS scavenging efficiency of the AuNCs formulated at the optimal 3:1:1 ratio (determined by Western blot) to evaluate the role of surface LA. To assess the intracellular ROS-scavenging capacity of PLANC, we utilized 2′,7′-dichlorodihydrofluorescein diacetate (DCFH-DA). DCFH-DA is a cell-permeable fluorogenic probe widely used to detect intracellular ROS levels. The ROS scavenging had the same significance with LA and LA-PEG-NH_2 spacers as well as the full PLANC system with no spacer (Figure S22). Increasing the amount of PEG conjugated to LA led to a slight, non-significant reduction in its antioxidant properties. Despite this scalable diminishment, all synthesized clusters demonstrated a statistically significant reduction in ROS. Through these initial screenings, the two best ligand compositions for PLANC to achieve the desired therapeutic effects were LA-PEG-Pom: LA-PEG-Tol blue: LA in a 1:1:3 ratio and LA-PEG-Pom: LA-PEG-Tol blue: LA-PEG-NH_2 in a 1:1:3 ratio. Subsequent concentration-dependent screenings indicated that both conditions enhanced cell survival, with viability recovering to similar levels as the negative control (Figure S23a,c). To determine the effects on protein degradation, western blot and protein staining were performed for both LA-PEG-Pom:LA-PEG-Tol blue:LA in a 1:1:3 ratio and LA-PEG-Pom:LA-PEG-Tol blue: LA-PEG-NH_2 in a 1:1:3 ratio in a concentration-dependent manner (Figure 3a–c; Figure S23e,f).

Thioflavin T (ThT) fluorescence assays were performed to validate the observed reduction in intracellular protein aggregates. ThT, a fluorescent dye that specifically binds to pTau aggregates, provides a reliable quantitative measure of protein aggregation. Triplicate measurements demonstrated a significant decrease in ThT fluorescence, confirming a substantial reduction in intracellular pTau aggregates (Figure S23b,d). Downregulation of pTau at serine 202/threonine 205 (S202/T205) was confirmed by western blot to determine which condition gave optimal protein degradation (Figure 3c; Figures S23 and S26). The housekeeping protein beta-actin was also stained to quantify pTau levels in cells relative to beta-actin levels (Figure 3b; Figures S23 and S26). Furthermore, cellular uptake of PLANC and LA AuNCs was successfully confirmed (Figure S23h). Rhodamine B isothiocyanate (RITC)-labeled PLANC uptake was studied in a time-dependent manner and showed significant uptake into the cells after only 4 h (Figure S24). Based on the combined results of cell viability, protein degradation, and ROS scavenging, the optimal ligand

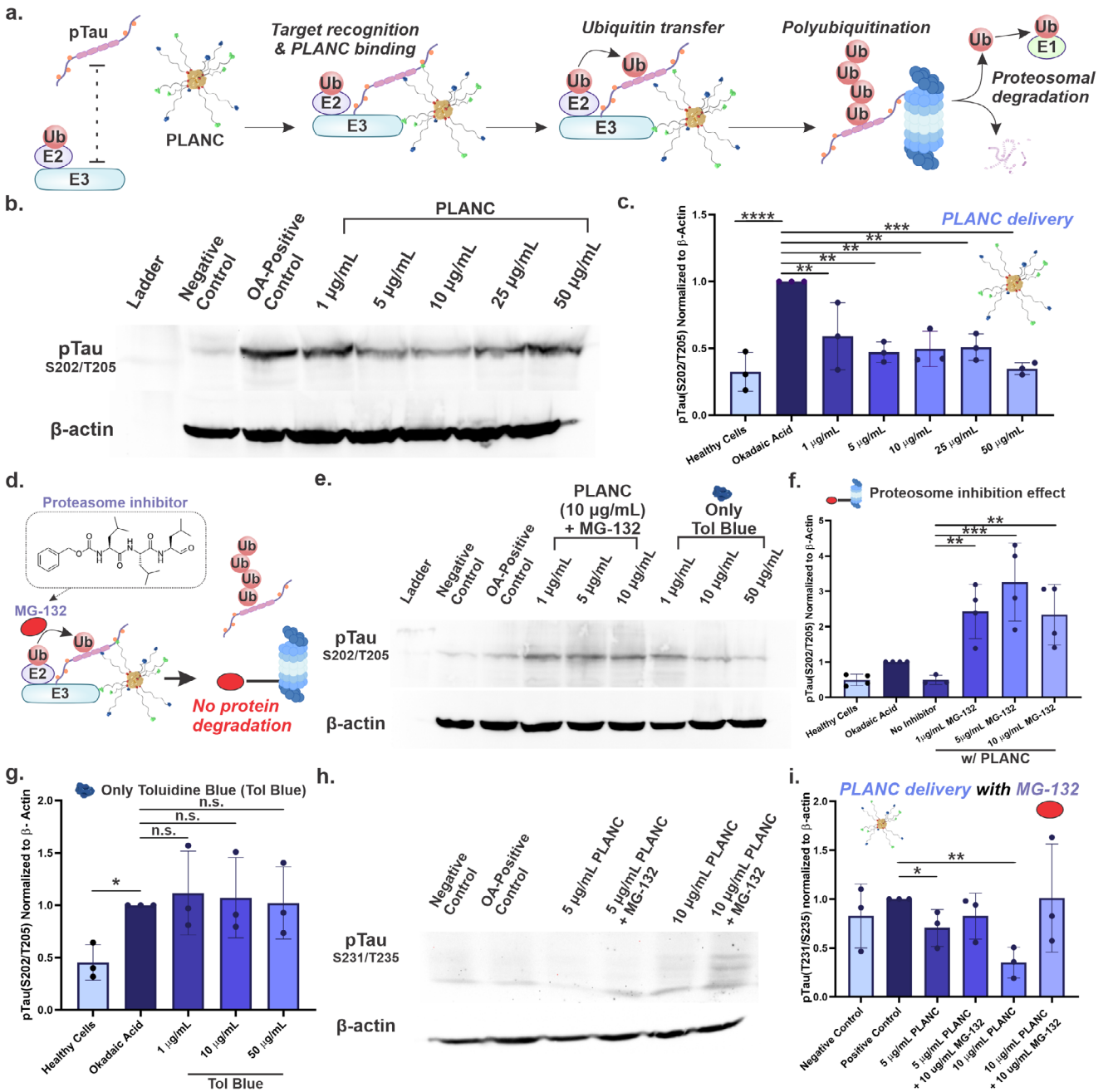

FIGURE 3 | (a) Mechanism of action for pTau degradation upon PLANC delivery. (b) Western Blot of pTau(S202/T205) with protein extracted from SH-Sy5y cells upon PLANC delivery. (c) Quantification of pTau(S202/T205) levels from western blot ($n = 3$). (d) Schematic showing MG-132 inhibition of the proteasome to prevent protein degradation. (e) Western blot analysis of free Toluidine Blue O delivery and co-delivery of MG-132 and PLANC in SH-SY5Y cells. (f) Quantification of protein levels following co-delivery of MG-132 and PROTAC LA AuNC ($n = 4$). (g) Quantification of protein levels following free Toluidine Blue O delivery ($n = 3$). (h) Western blot of pTau (T231/S235) with protein extracted from SH-Sy5y cells upon PROTAC LA AuNC delivery. (i) Quantification of pTau (T231/S235) protein levels from western blot ($n = 3$). Data are mean ± standard deviation; $^{*}p < 0.05$, $^{**}p < 0.01$, $^{***}p < 0.001$, $^{****}p < 0.0001$ for figure 3c,f,g, and i by one-way ANOVA with Tukey post-hoc analysis.

condition for PLANC was determined to be LA-PEG-Pom: LA-PEG-Tol blue: LA in a 1:1:3 ratio. Therefore, careful optimization of the **LA:LA-PEG-Pom:LA-PEG-Tol blue** ratio was essential to maximize PLANC's efficacy in degrading pTau and mitigating inflammation. One of the key advantages of the PLANC system is its modularity.

To continue testing the finalized PLANC system, flow cytometry was used to verify the results of PLANC delivery and showed an increase in the percent of cells with a low pTau(S202/T205) signal (<1000), as well as a decrease in the percent of cells with a high pTau signal (>1000) across all concentrations of PLANC delivery (Figure S25). To claim the proteasome as the mechanism of pTau reduction, several controls were required. Cells were treated with Tol blue delivered by PLANC in the presence and absence of the proteasome inhibitor MG-132. pTau (S202/T205) levels were then quantified relative to beta-actin. PLANC co-delivery with MG-132 led to a significant increase in pTau levels higher than

OA alone (Figure 3e,f; Figure S26), giving evidence that MG-132 inhibits PLANC function as well as eliminates natural protein degradation by the proteasome. Total protein levels are also given (Figure S27). Tol blue delivery alone, which binds to pTau, led to no significant changes in pTau levels (Figure 3e,g; Figure S26), confirming the inability to degrade tau without Pom binding to the E3 Ligase. Protein degradation in a time-dependent manner was studied with western blot at 6, 12, 24, and 48 h as other studies were all conducted at 24 h (Figure S28). To further study time-dependence, MG-132 was co-delivered with PLANC in a separate time-dependent experiment to show proteasome-dependent protein degradation overtime, which showed significant degradation of pTau at 8 and 24 h after PLANC delivery unless MG-132 was co-delivered (Figure S29). Following PLANC and MG-132 co-delivery, pTau levels did not decrease. Furthermore, there was a significant increase in pTau levels from PLANC treated cells to PLANC + MG-132 treated cells at 24 h. Western blot was also run on pTau(S231/T235) to confirm the degradation of other isoforms critical to AD, and results showed that pTau(T231/S235) levels were significantly downregulated with PLANC delivery alone (Figure 3h; Figure S26). However, no significant difference in pTau protein levels was observed when PLANC was co-delivered with MG-132 compared to OA-treated cells, further supporting the role of UPP in PLANC-mediated degradation (Figure 3h,i; Figure S26). Finally, to confirm the effects of PLANC versus a small molecule PROTAC, Pom-PEG4-Tol blue was synthesized, and a western blot was run (Figure S30a,b). The western blot results confirmed that pTau degradation was less effective than PLANC with the same μg/mL delivered (Figure S30c).

2.3 | Using iPSC-NPCs to Investigate PLANC Effects in Mature Neurons Induced with pTau

To further evaluate the therapeutic potential of PLANC in a more physiologically relevant setting, we utilized human-induced pluripotent stem cell-derived neuroprogenitor cells (iPSC-NPCs). These iPSC-NPCs were differentiated into mature neurons and subsequently treated with OA to induce pathological conditions mimicking those observed in AD. Following OA treatment, the neurons were treated with PLANC to assess therapeutic effects (Figure 4a; Figure S31a). While there are some differences from mature neurons differentiated from iPSC-NPCs and neurons isolated from a brain, differentiated iPSC-NPCs are a commonly used cell model to study AD and other brain related diseases due to the difficulty of obtaining isolated human neurons [68]. Cell viability and ROS scavenging assays were conducted, demonstrating that PLANC delivery did not affect cell viability while effectively reducing ROS levels (Figure 4i; Figure S31b). Treatment with OA significantly reduced cell viability compared to the negative control group. However, PLANC treatment effectively restored cell viability to near-negative control levels. After delivery of RITC-labeled PLANC for 24 h, cell uptake was confirmed (Figure S31d). Western blot was run on protein extracted from the mature neurons after inducing pTau formation with OA and treating PLANC or LA AuNCs at both 5 and 10 μg/mL. The results confirmed significant downregulation of pTau(T231/S235) with PLANC at both concentrations (Figures S31e and S32). LA AuNCs led to less significant downregulation of pTau(T231/235) at both 5 and 10 μg/mL (Figures S31e,f; Figure S32). The internalization of PLANC into neurons was determined to be diffusion-based via uptake experiments at 4°C (Figure S31g,h). Western blot was run on NOX4, pTau(s396), and Tau(46) to iPSC-NPCs induced with OA and incubated with PLANC in a concentration-dependent manner (Figure 4c; Figure S33). A significant decrease in Tau(46), pTau(S396), and NOX4 levels was observed across all conditions after PLANC delivery (Figure 4d–f). Immunostaining of pTau also revealed a significant decrease in fluorescent signal for all PLANC conditions relative to OA-treated cells (Figure 4g,h). RT-q-PCR was used to confirm mRNA expression relative to *gapdh* levels following PLANC delivery to OA-treated cells. Overall, there was significant downregulation in *gsk-3β*, *nf-κb mtor*, *akt*, and *il-1β* with PLANC treatment at 5 μg/mL, the optimal concentration for therapeutic effects in iPSC-NPCs (Figure 4b).

2.4 | Targeting Neuroinflammation and Neurodegeneration: Assessing PLANCs Effects in Neuronal and Glial Cell Models

To gain a deeper understanding of PLANC's effects on cell–cell interactions within a more physiologically relevant context, we developed a co-culture system with THP-1 cells differentiated into macrophages and iPSC-NPCs differentiated into mature neurons. By implementing this co-culture model, we evaluated the therapeutic effects of PLANC within a more dynamic and complex cellular environment, capturing some of the key interactions between neurons and immune cells in the brain (Figure S34a,b). It was determined that adding THP-1 cells to the differentiating iPSC-NPCs in a 1:1 ratio on day 8 of differentiation led to good cell viability and low expression of CD40, an inflammatory surface receptor, on THP-1 cells (Figure S35). A reduction in CD40 expression upon PLANC delivery was confirmed with immunostaining, illustrating the anti-inflammatory effects on macrophages (Figures S34c,d; Figure S36). The PLANC system offers a multifaceted approach to AD treatment by not only preventing NFT formation and degrading pTau but also scavenging ROS. This multi-targeted strategy holds promise for effectively addressing the complex and interconnected pathologies of AD. CD-40 expression has been implicated in AD as connected to pTau formation, inflammation, and Aβ plaque formation [69, 70]. PLANC's ability to lower CD-40 expression on macrophages suggests it could significantly alter the brain's microenvironment, offering a potential AD treatment. In addition, macrophage uptake of PLANC was confirmed in a time-dependent manner in a monoculture (Figure S37).

PLANC was delivered to primary human astrocytes to better study effects on the brain environment and further confirm anti-inflammatory effects (Figure 5a) [71–73]. After directing astrocytes toward a pro-inflammatory state, PLANC was delivered for 24 h, and there was no significant change in cell viability for all conditions (Figure S38a). RT-q-PCR showed a significant downregulation in *gsk-3β, bax, il-1β*, and a significant upregulation in *tgf-β* after treatment with 10 μg/mL PLANC (Figure S39). RT-q-PCR also confirmed a downward trend in *nf-κb* RNA levels and an increase in *bcl2* (Figure S38b,c). Immunofluorescent imaging revealed NF-κB translocated to the nucleus in a pro-inflammatory environment and initiated the signaling of pro-inflammatory molecules (Figure S40a). Quantification of images confirmed that PLANC also led to a significant decrease in the nuclear co-localization of NF-κB at 10 μg/mL (Figure S40b). The increase in

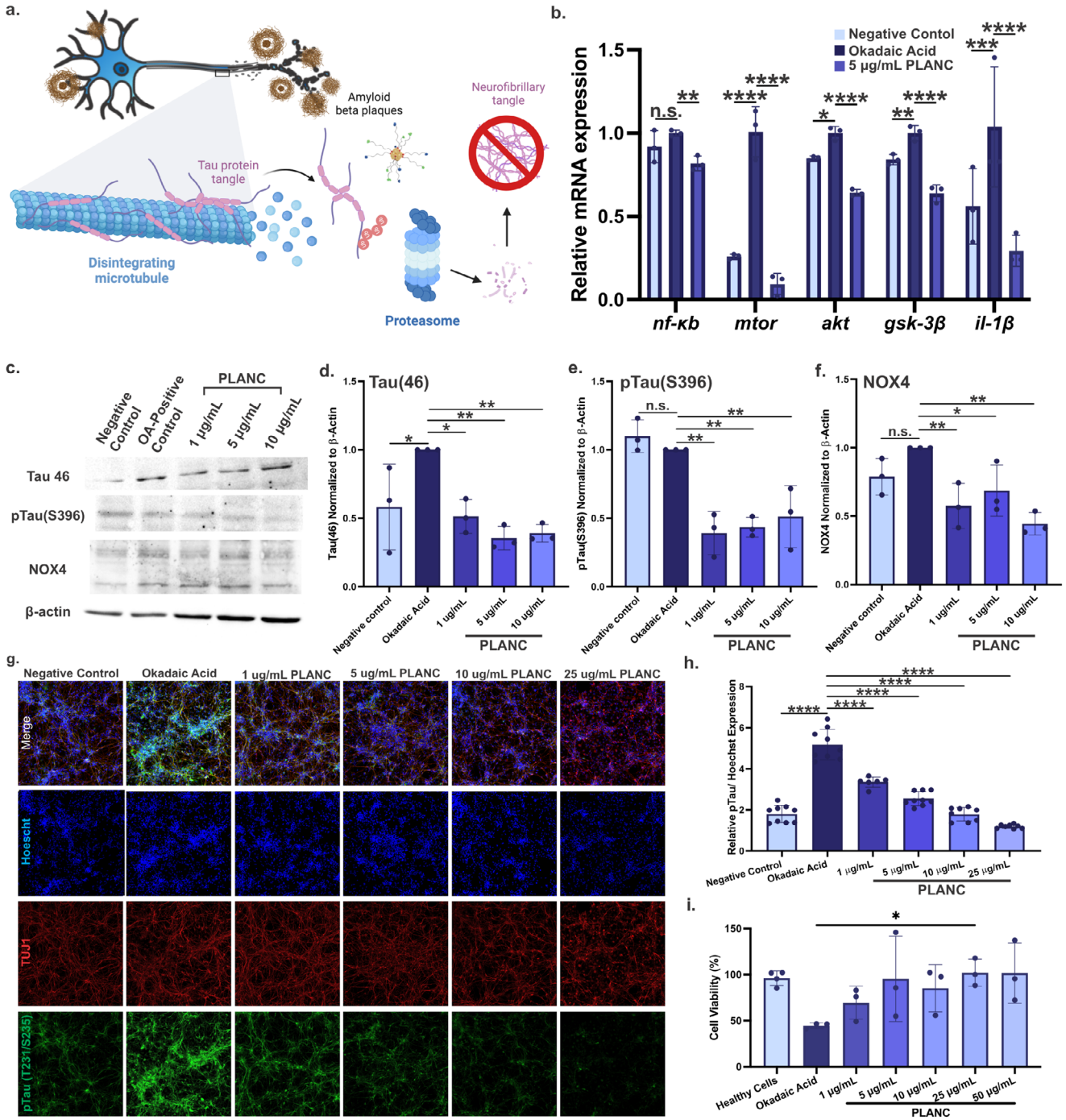

FIGURE 4 | (a) Schematic of PLANC effects on mature neurons induced with okadaic acid. (b) Rt-q-PCR of controls and PLANC at 5 µg/mL for NF-κB, mTOR, AKT, GSK-3β, and IL-1β with significance determined by two-way ANOVA with Tukey post-hoc analysis ($n = 3$). (c) Western Blot of tau 46, pTau S396, and NOX4. (d) Quantification of tau 46 with significance determined by one-way ANOVA with Tukey post-hoc analysis ($n = 3$). (e) Quantification of pTau S396 with significance determined by one-way ANOVA with Tukey post-hoc analysis ($n = 3$). (f) Quantification of NOX4 with significance determined by one-way ANOVA with Tukey post-hoc analysis ($n = 3$). (g) Immunostaining of pTau(S202/T205), TUJ1, and Hoechst. (h) Quantification of pTau(S202/T205) immunostaining images by one-way ANOVA with Tukey post-hoc analysis ($n = 9$). (i) Cell viability in okadaic acid-induced iPSC-NPCs by one-way ANOVA with Tukey post-hoc analysis ($n = 3$). Data are mean ± standard deviation; *$p < 0.05$, **$p < 0.01$, ***$p < 0.001$, ****$p < 0.0001$ by one-way or two-way ANOVA with Tukey post-hoc analysis.

NF-κB co-localization with the nucleus of astrocytes after TNF-α and IFN-γ delivery shows that it is signaling the transcription of pro-inflammatory cytokines. PLANC delivery led to a higher NF-κB expression in the cytoplasm and a decrease in NF-κB nuclear translocation, indicating a decrease in NF-κB signaling of pro-inflammatory cytokines. We have also performed flow cytometry with NOX4 and IL-1B to confirm anti-inflammatory effects on an individual cell basis (Figure 5a,b). To further study the anti-inflammatory effects of PLANC in astrocytes, CASP3, IL-1β, and LAMP1 levels were further quantified relative to β-actin

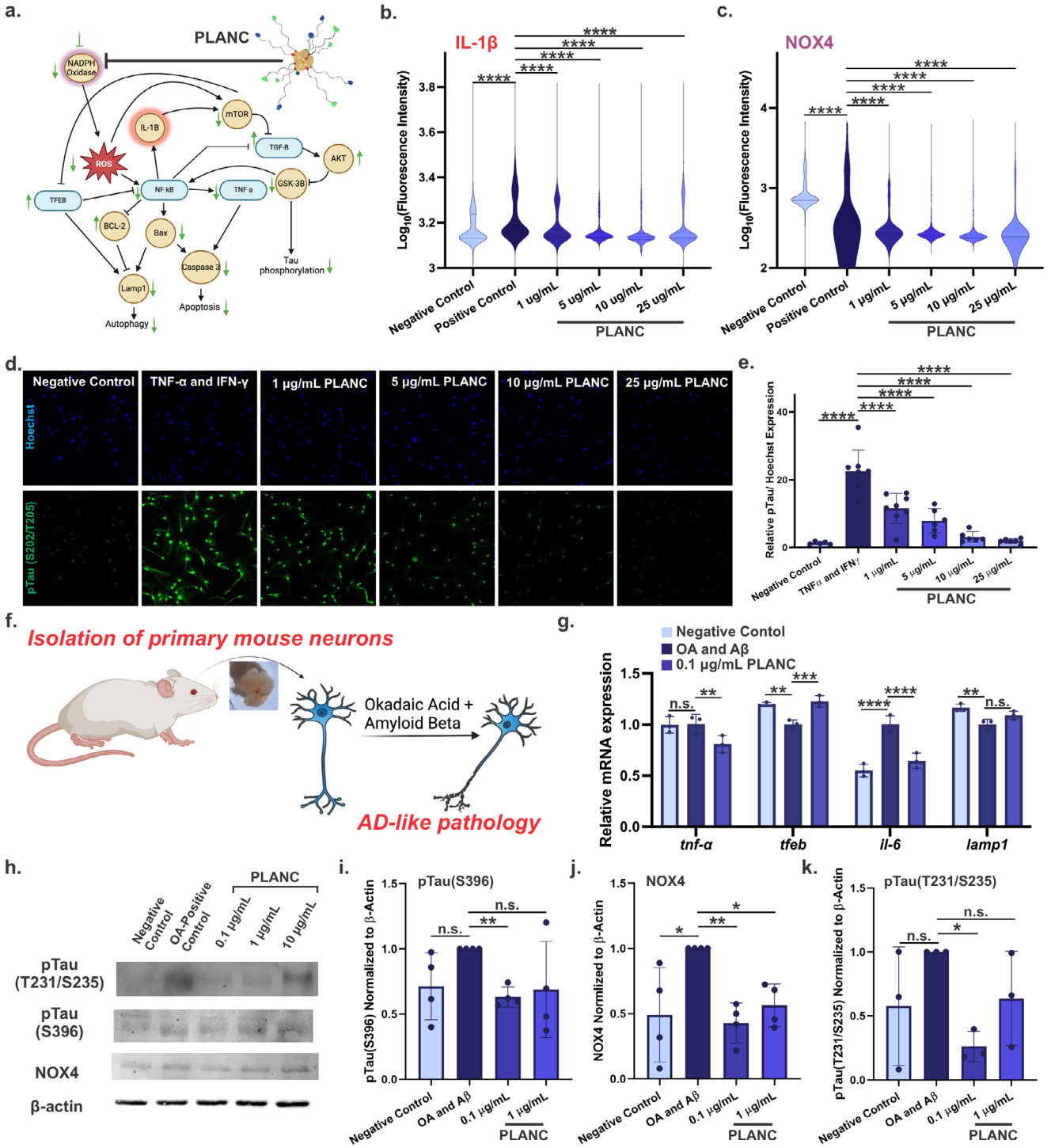

FIGURE 5 | (a) Pathway of proposed PLANC mechanism of action on inflammation. (b) Flow cytometry of IL-1β and (c) NOX4 with significance determined by one-way ANOVA with Tukey post-hoc analysis. (d) pTau(S202/T205) Immunostaining and (e) quantification by one-way ANOVA with Tukey post-hoc analysis ($n = 5$–8). (f) Schematic of primary neuron isolation from a mouse. (g) RT-q-PCR of *tnf-α, tfeb, il-6*, and *lamp1* with significance determined by two-way ANOVA with Tukey post-hoc analysis ($n = 3$). (h) Western Blot Images of pTau(T231/S235), pTau(S396), and NOX4 protein levels. (i) Quantification of pTau (S396) protein levels by one-way ANOVA with Tukey post-hoc analysis ($n = 3$). (j) Quantification of NOX4 protein levels by one-way ANOVA with Tukey post-hoc analysis ($n = 4$). (k) Quantification of pTau(T231/S235) protein levels by one-way ANOVA with Tukey post-hoc analysis ($n = 4$). Data are mean ± standard deviation; $^{*}p < 0.05$, $^{**}p < 0.01$, $^{***}p < 0.001$, $^{****}p < 0.0001$.

with western blot, and all three proteins were downregulated (Figures S41 and S42). To assess the impact of PLANC on tau phosphorylation in astrocytes, we performed immunostaining for pTau (S202/T205). Quantification of the immunofluorescence signal revealed a significant reduction in pTau levels following PLANC treatment (Figure 5d,e). This indicates the effectiveness of PLANC in targeting and decreasing pTau in astrocytes (Figure 5d,e). IL-1β and cleaved caspase 3 immunostaining also confirmed the downregulation of both protein levels with increasing concentrations of PLANC (Figure S38e). Primary mouse neurons were isolated and co-delivered with OA and amyloid beta (Aβ) to induce an AD-like pathology and give a more representative model for the disease (Figure 5f). The cell viability assay showed no significant change with any condition (Figure S38d).

PLANC led to significant downregulation of pTau levels and inflammatory cytokine levels at a much lower concentration in the primary mouse neurons (Figure 5g). At 0.1 μg/mL, PLANC caused a significant reduction in *tnf-α* and *il-6*, and a substantial increase in *tfeb* RNA levels in the neurons (Figure 5g). Significant changes in key mRNA were also linked to AD-related inflammation in astrocytes and primary neurons following PLANC delivery. This further illustrates the ability of PLANC to regulate pro-inflammatory cytokines in cell types critical to the AD environment. *Il-1β*, *nf-κb*, *mtor*, *tnf-α*, *il-6*, and *bax* were all downregulated, while *tgf-β* and *tfeb* were significantly upregulated. By examining various mRNA-related pathways influenced by LA interactions with cells, we identified significant changes in the expression levels of *bax* and *casp-3*, both of which play critical roles in autophagy. Casp-3 is also a key enzyme for apoptosis. Immunostaining further validated these findings, confirming their involvement in the cellular processes modulated by PLANC. *mtor* was downregulated in neurons differentiated from iPSC-NPCs, which helps to regulate key pro-inflammatory cytokines, such as *gsk-3β*, which was also significantly downregulated. The decreased NF-κB co-localization with the nucleus and overall lower intracellular levels quantified with RT-q-PCR also confirmed effects on that inflammatory pathway. *il-1β* downregulation is highly connected to both NF-κB located in the cytoplasm and *mtor* downregulation. Testing the effects of PLANC in mature neurons from iPSC-NPCs, primary human astrocytes, and primary mouse neurons showed the clinical potential of PLANC, as it can help regulate inflammation in primary cells that are key to AD.

Western blot was used to confirm a significant reduction in pTau(S231/T235), pTau(S396), and NOX4 protein levels in Aβ and okadaic acid-induced primary mouse neurons after treatment with 0.1 μg/mL PLANC (Figure 5h–k; Figure S43). Testing the degradation of multiple types of pTau (S202/T205, T231/S235, S396), and total tau in multiple cell types (SH-Sy5y cells, iPSC-NPCs, primary human astrocytes, and primary mouse neurons) with western blot and immunostaining shows the potential of this system for significant pTau degradation that is consistent across many cell lines and primary cells. Regulation of inflammatory factors is a key goal because of the role of inflammation in AD. NOX4 helps regulate inflammatory pathways and is dysregulated in AD [74]. According to the literature, LA can directly interact with NADPH oxidase, scavenge ROS, and regulate a multitude of inflammatory factors downstream [37, 75, 76]. The marked downregulation of NOX4, a key NADPH oxidase subunit, at both the mRNA and protein levels supports the role of LA in modulating neuronal responses.

2.5 | Evaluating Blood-Brain Barrier Permeability of PLANC Using a Transwell System

To investigate the ability of PLANC to penetrate the BBB, we established an in vitro BBB model using a transwell system. This model incorporated a co-culture of primary human astrocytes and human umbilical vein endothelial cells (HUVECs) grown on a porous membrane with a pore size of 0.4 μm (Figure 6a). To confirm PLANC effects on HUVEC viability, PLANC was delivered in a time and concentration-dependent manner to HUVECs and there was no significant change in viability for any concentration up to 50 μg/mL or for up to 72 h with 50 μg/mL PLANC (Figure S44). The densities of both astrocytes and endothelial cells were carefully optimized to ensure complete coverage of the membrane, thereby creating a tight barrier that accurately mimics the in vivo BBB (Figure S45). 40 kDa FITC-Dextran was used to initially confirm proper barrier formation. To further verify the formation of tight junctions between the astrocytes and endothelial cells in our BBB transwell model, we performed immunostaining for the tight junction proteins ZO-1 and occludin (Figure 6b; Figure S46). Staining allowed for clear visualization of the two cell types and confirmation that tight junction formation occurred at the endothelial cell–cell interface in the presence of astrocytes, highlighting their role in enhancing BBB integrity.

Next, to compare PLANC with other PROTAC systems, a larger PROTAC AuNP was synthesized and delivered, as well as the Pom-PEG4-Tol Blue, small molecule PROTAC, described and characterized earlier. The larger PROTAC AuNP was characterized by UV–vis and DLS (Figure S47). The DLS data showed the AuNPs average size to be 51 nm with a PDI of 0.191. RITC-labeled PLANC, Pom-PEG4-Tol blue, PROTAC AuNPs and FITC-Dextran delivery were monitored overtime to compare PLANC passage through the in vitro BBB model to control conditions (Figure 6c–f; Figure S48). A standard curve was made with known concentrations of RITC-PLANC, Pom-PEG4-Tol blue, PROTAC-AuNPs, and FITC-Dextran to quantify the amount allowed to pass through the BBB (Figure S48). PLANC or control conditions were delivered at a concentration of 50 μg/mL to the apical side of the transwell, and the fluorescence intensity on the basolateral side was monitored over time. This allowed for assessing PLANC's ability to traverse the BBB model. After 24 h, only 13.3% of the Pom-PEG4-Tol blue and 34.8% of the PROTAC AuNP that passed the empty transwell passed the BBB model, in comparison to 70.2% of PLANC that passed the empty transwell passed the BBB model as well (Figure 6c–f). At 72 h, 55.6% of PLANC that was able to pass through the empty transwell passed through the BBB transwell model. At the same time, only 29% of FITC-Dextran, 33.8% of the PROTAC AuNP, and 36.4% of the Pom-PEG4-Tol blue that had passed through the empty transwell could pass through the BBB model (Figure 6c). This significant increase in PLANC passage of the BBB model over control conditions illustrates its potential. The lack of FITC-dextran, Pom-PEG4-Tol blue, and PROTAC AuNP that passed the BBB transwell model relative to RITC-labeled PLANC shows that it is acting to prevent standard molecules from passing due to strong barrier formation.

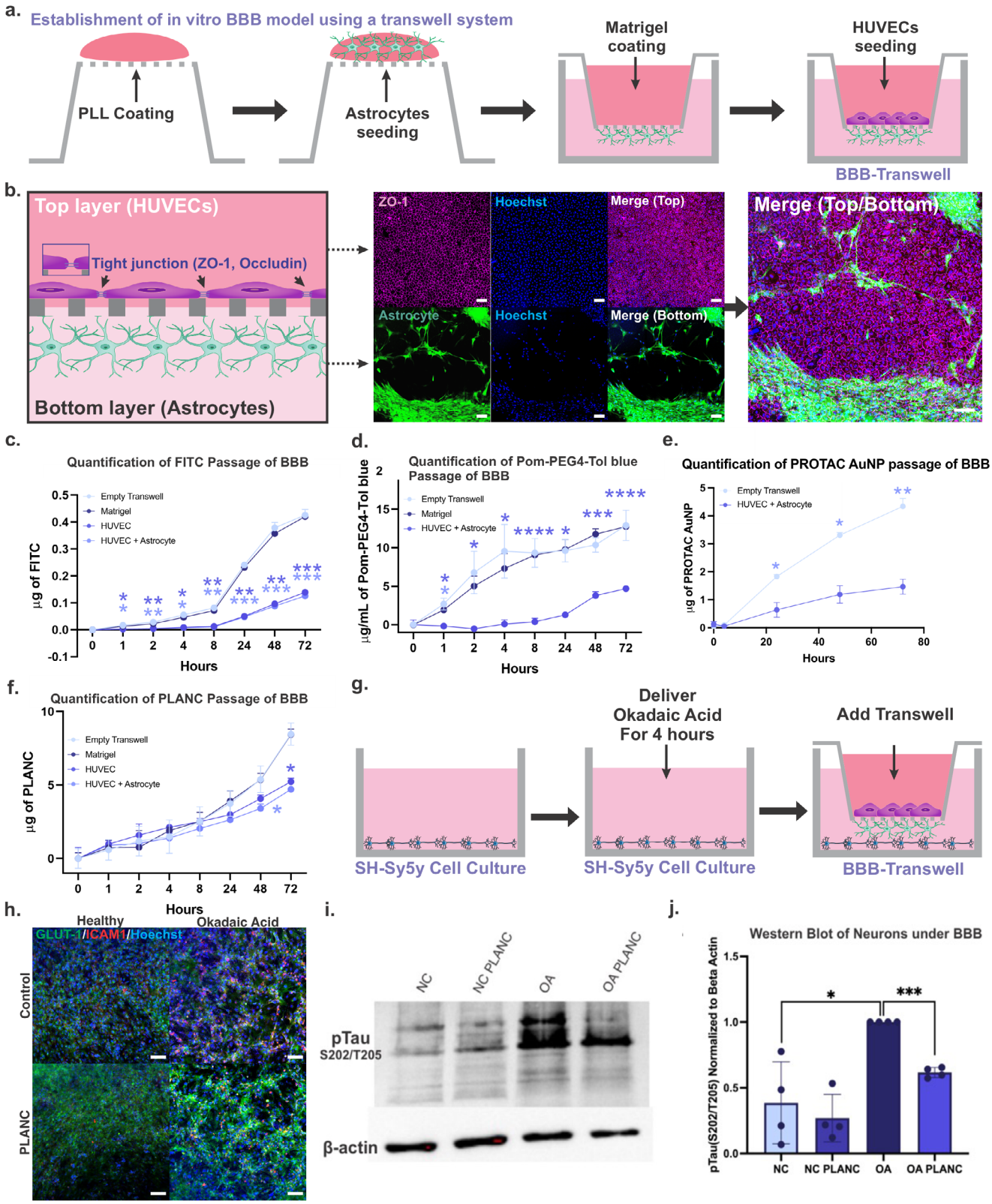

FIGURE 6 | (a) Schematic of BBB transwell model development. (b) Tight junctions in the BBB with immunostaining of red cell tracker-labeled HUVECs, Hoechst, ZO-1(Alexa fluor 647), and green cell tracker-labeled astrocytes. (c) Quantification of 40 kDa FITC-Dextran passage of in vitro BBB based on the standard curve with significance comparing the HUVECS + Astrocytes and HUVECs alone to the empty transwell at each time point by two-way ANOVA with Tukey post-hoc analysis ($n = 3$). (d) Quantification of Pom-PEG4-Tol Blue passage of in vitro BBB based on the standard curve with significance comparing the HUVECS + Astrocytes and HUVECs alone to the empty transwell at each time point by two-way ANOVA with Tukey post-hoc analysis ($n = 3$). (e) Quantification of PROTAC AuNP passage of in vitro BBB based on the standard curve with significance comparing the HUVECS + Astrocytes and HUVECs alone to the empty transwell at each time point by two-way ANOVA with Tukey post-hoc analysis ($n = 3$).(f) Quantification of PLANC passage of the in vitro BBB based on the standard curve with significance comparing the HUVECs + Astrocytes to the empty

A two-way ANOVA statistical analysis with a post-hoc Tukey test was performed to see if there was a significant difference in the passage of each transwell condition over time for RITC-PLANC, FITC-Dextran, Pom-PEG4-Tol Blue, and PROTAC AuNP. Significantly less of each control condition passed through the model with cells then the empty transwell at all tested time points illustrating the model's effectiveness (Figure 6c–f). Furthermore, there was no significant decrease in the amount of RITC-PLANC passing through the model with cells compared to the empty transwell until 72 h after delivery (Figure 6f). This enhanced transport may primarily be attributed to PLANC's small size and surface properties. These findings highlight the potential of PLANC to effectively reach therapeutic targets within the brain. 31.4% of PLANC successfully traversed the in vitro BBB model through passive diffusion, a mechanism validated by the confirmed passage of PLANC through the transwell at 4°C when cellular processes are halted [77] (Figure S49). While there was slightly less passage through the transwell model at 4°C than 37°C, the significant increase in fluorescence overtime shows the same mechanism was utilized (Figure S49). Overall, PLANC passage through diffusion verifies BBB tight junctions do not prevent PLANC passage due to its ultra-small size. Further testing in vivo would allow for confirmation of BBB passage. Finally, to show that pTau degradation still occurs through the BBB transwell model, either healthy or OA-induced SH-Sy5y cells were seeded on the bottom of a plate and the transwells were placed in the wells. After delivering PLANC to the apical side of the transwell, the transwells were removed after 24 h, and western blot was conducted (Figure 6g). The OA-induced cells had significant pTau upregulation from the negative control, and there was also significant pTau downregulation in OA-induced SH-Sy5y cells after PLANC delivery (Figure 6h). While BBB passage is critical for the treatment of AD, there are discrepancies in BBB function between healthy individuals and AD patients, including loss of tight junction proteins leading to the facilitated passage of toxic species into the brain [78, 79]. By adding OA to the SH-Sy5y cells to induce pTau formation, we aimed to better replicate the disease state with our model. Moreover, ICAM1, which has been shown to be upregulated in AD, contributes to an increase in loss of tight junctions, reduces barrier function, as well as contributes to a change in endothelial cell morphology and TNF-α-induced vascular leakage [80]. GLUT1, which is significantly downregulated in endothelial cells in AD, leads to cerebral microvascular breakdown and BBB breakdown [81]. Therefore, immunostaining of GLUT1 and ICAM1 was performed on the endothelial cells in transwell models with healthy or OA-induced SH-Sy5y cells with and without PLANC delivery (Figures S50 and S51). This allowed for studying the effects of pTau-induced SH-Sy5y cells on BBB function, as well confirmed that PLANC delivery did not increase endothelial cell activation in the healthy or OA-induced BBB model. The imaging of a large area of the transwell through stitching together nine images showed that ICAM1 levels increased in endothelial cells after incubation with OA-induced SH-Sy5y cells. Furthermore, PLANC delivery to both the healthy and OA-induced model showed slightly less ICAM1 expression. This is most likely because ICAM1 expression is activated through NF-κB translocation to the nucleus and TNF-α and IL-1β activation which PLANC can regulate, as shown with our immunostaining and PCR data in astrocytes and neurons [82–84]. GLUT1 did not have any obvious changes between the healthy and OA-induced model, although there may have been a slight increase in expression upon PLANC delivery which would be beneficial for AD treatment (Figure S50). Furthermore, immunostaining of tight junctions showed similar expression for control and PLANC treated healthy BBB models while the OA-induced model led to a decrease in occludin expression (Figure S51). Therefore, the addition of OA-induced SH-Sy5y cells to the bottom of the BBB transwell model allows for better mimicking the BBB in the AD state. While the AD BBB model better mimics the disease environment to confirm therapeutic effects of PLANC, BBB dysfunction in AD has also been shown to be sporadic, in that it cannot be relied on for the passage of therapeutics to the brain in all cases [85]. Overall, PLANC passage was tested through a healthy BBB model to confirm the feasibility of delivery without BBB disruption. Furthermore, due to the diffusive mechanism of PLANC in the context of BBB passage, we hypothesize that tight junction disruption would lead to an increase in PLANC delivery through the BBB.

Because of their size, the involvement of AuNCs in renal clearance has been demonstrated, indicating that the next important step to show clinical translation is to test PLANC renal clearance in vivo [33, 86]. As most studies were done with human cells to look at clinical translation potential, primary mouse neurons isolated from an embryonic mouse brain were used to further test PLANC effects in mouse cells. The significant downregulation of pTau (S396) and pTau (S231/T235), along with reduced NOX expression in mouse cells treated with OA and mouse Aβ, together with the demonstrated potential for BBB penetration, emphasizes the promise of PLANC for therapeutic efficacy in an in vivo AD mouse model. Some limitations of this system that should be addressed in future work include hemolysis and plasma protein absorption studies, targeted delivery to the brain, and testing renal clearance in vivo. Potential methods for delivery of PLANC to the brain include intravenous delivery and intranasal delivery. Future testing of PLANC in an in vivo AD model would help further confirm the therapeutic potential of PLANC for AD.

3 | Conclusion

In this study, we designed and developed **PLANC**, a novel, multifunctional nanotherapeutic platform meticulously engineered to concurrently address several key pathological hallmarks of AD. The complex and multifactorial nature of AD, involving protein

transwell at each time point by two-way ANOVA with Tukey post-hoc analysis ($n = 3$). (g) Schematic of BBB model including OA-induced SH-Sy5y cells. (h) Immunostaining of GLUT-1/ICAM1/Hoescht (scale bar = 100μm). (i) Western blot of pTau in SH-Sy5y cells under the BBB transwell model. (j) Quantification of pTau degradation in healthy and OA-induced SH-Sy5y cells under the transwell model by one-way ANOVA with Tukey post-hoc analysis ($n = 4$). For all statistical analysis, data are mean ± standard deviation; *$p < 0.05$, **$p < 0.01$, ***$p < 0.001$, ****$p < 0.0001$ for all statistical analysis.

aggregation, neuroinflammation, and oxidative stress, presents a significant challenge for conventional single-target therapies. Our platform directly confronts this challenge by synergistically integrating three distinct therapeutic modalities into a single, cohesive entity: (i) *Systematically designed and synthesized ligands*, which hijacks the endogenous ubiquitin-proteasome system to induce the selective and highly specific degradation of pathogenic pTau, (ii) *the potent antioxidant and anti-inflammatory agent LA*, which is covalently conjugated to the platform to neutralize ROS and downregulate pro-inflammatory cytokine signaling, and (iii) *ultra-small gold nanoclusters (AuNCs)*, which act as a nanoscale delivery vehicle to enhance the stability and cellular uptake of the therapeutic components while facilitating penetration across the BBB. By uniting these functions, PLANC represents a significant advancement over strategies that address these pathological pathways in isolation, offering a holistic approach to AD treatment. AD has different staging for the spreading of amyloid beta and tau pathology. As previously mentioned, Braak staging is used to determine the tau spreading and further progression is correlated with the expansion of pTau pathology to specific regions of the brain. Considering AD pathology in clinical settings, PLANC treatment has the potential for therapeutic effects across Braak stages as tau spreading occurs. In Braak stages I and II, PLANC has the potential to prevent neurofibrillary tangle formation, tau spreading, and neuronal death through pTau degradation and anti-inflammatory properties in the transentorhinal and entorhinal cortexes in the medial temporal region of the brain. In later Braak stages, PLANC will hypothetically have the same therapeutic effects, but pTau pathology includes NFT formation as cell to cell spreading of tau occurs from the medial temporal regions (Braak I-II) to the limbic regions (Braak III-IV) and finally to the whole cortical mantle (Braak V-VI) [87]. Therefore, in later Braak stages, PLANC would be beneficial for reducing pTau levels in multiple regions of the brain. Finally, across all Braak stages, reducing inflammatory levels would be extremely helpful to work synergistically with pTau degradation to prevent cell to cell spreading through inflammatory cells known to help in pTau propagation through the brain. According to experimental data collected, PLANC was uptake into astrocytes for the degradation of pTau and reduction inflammatory effects which is extremely relevant for the potential of reducing pTau as astrocytes help propagate the spreading of pTau [88].

The therapeutic efficacy and mechanistic action of the PLANC platform were systematically validated across a variety of relevant cell culture systems, including human neuroblastoma SH-SY5Y cells and primary cortical neurons, confirming its robustness and broad applicability. Our results demonstrate that PLANC formulation significantly enhanced the degradation of pTau compared to the PROTAC molecule alone, indicating a synergistic effect conferred by the AuNC scaffold. Similarly, the platform exhibited superior antioxidant and anti-inflammatory properties compared to LA alone, effectively scavenging ROS and reducing the expression of key pro-inflammatory markers. A critical achievement of this work was the demonstration of PLANC's ability to traverse a restrictive in vitro BBB model. PLANC exhibited substantial transcytosis, significantly outperforming the macromolecular control, FITC-dextran, which showed minimal passage. This result is paramount, as the inability to cross the BBB is a primary cause of failure for many promising central nervous system therapeutics. As each component contributes to a multifaceted therapeutic effect, these comprehensive validation studies confirm PLANC functions as an integrated system with an effect that is greater than the sum of its individual parts.

While this study provides compelling preclinical evidence for the translational potential of PLANC, further investigation involving in vivo animal models of AD is warranted to rigorously establish its therapeutic efficacy, biodistribution, and long-term safety profile. Looking forward, a key advantage of the PLANC platform is its inherent **modularity**. The design allows for the straightforward substitution of the pTau-binding moiety (toluidine blue) with alternative small molecules that target other pathogenic proteins. This "plug-and-play" capability enables the platform to be rapidly adapted for the treatment of other neurodegenerative disorders characterized by protein aggregation, such as targeting α-synuclein in Parkinson's disease or huntingtin in Huntington's disease. Future efforts will focus on expanding this library of targeting ligands and optimizing the platform for in vivo administration. Ultimately, we envision PLANC as a versatile and transformative paradigm in nanomedicine, with the potential to shift the treatment of neurodegenerative diseases from single-target symptom management to a holistic, multipronged strategy that addresses the interconnected and core drivers of neurodegeneration.

Acknowledgements

Ki-Bum Lee acknowledges the partial financial support from the New Jersey Commission on Spinal Cord (CSCR16ERG019; CSCR24IRG005), NIH R01 (1R01NS130836-01A1), NIH RM1 (RM1 NS133003-01), CDMRP (OCRP, OC220235P1), New Jersey Commission on Brain Injury Research (CBIR25IRG005; CBIR25IRG015), and Alzheimer's Association (AARG-NTF-21-847862). S.N. acknowledges fellowship support as part of the NIH T32 Biotechnology Training Program (GM135141). B.C. acknowledges fellowship support as part of the NIH T32 Training in Translating Neuroscience to Therapies Program (5T32NS115700-02). Some graphics were created with BioRender.com. Thank you to Dr. Srinivas Chakravartula for the guidance and assistance with ESI-MS. Thank you to Dr. Phil Batson for advice and training on Ultra-STEM and EELS.

Conflicts of Interest

The authors declare no conflicts of interest.

Data Availability Statement

The data that support the findings of this study are available from the corresponding author upon reasonable request.

References

1. M. Calabro, C. Rinaldi, G. Santoro, and C. Crisafulli, "The Biological Pathways of Alzheimer Disease: A Review," *AIMS Neuroscience* 8 (2021): 86.

2. Z. Chen and C. Zhong, "Oxidative Stress in Alzheimer's Disease," *Neuroscience Bulletin* 30 (2014): 271–281.

3. S. Giorgetti, C. Greco, P. Tortora, and F. A. Aprile, "Targeting Amyloid Aggregation: An Overview of Strategies and Mechanisms," *International Journal of Molecular Sciences* 19 (2018): 2677.

4. A. D. Alonso, T. Zaidi, M. Novak, H. S. Barra, I. Grundke-Iqbal, and K. Iqbal, "Interaction of Tau Isoforms With Alzheimer's Disease Abnormally

Hyperphosphorylated Tau and in VitroPhosphorylation into the Disease-Like Protein," *Journal of Biological Chemistry* 276 (2001): 37967–37973.

5. K. Ando, S. Houben, M. Homa, et al., "Alzheimer's Disease: Tau Pathology and Dysfunction of Endocytosis," *Frontiers in Molecular Neuroscience* 13 (2020): 583755.

6. C. Ising, C. Venegas, S. Zhang, et al., "NLRP3 Inflammasome Activation Drives Tau Pathology," *Nature* 575 (2019): 669–673.

7. A. S. Chesser, S. M. Pritchard, and G. V. Johnson, "Tau Clearance Mechanisms and Their Possible Role in the Pathogenesis of Alzheimer Disease," *Frontiers in Neurology* 4 (2013): 122.

8. S. Guha, G. V. W. Johnson, and K. Nehrke, "The Crosstalk Between Pathological Tau Phosphorylation and Mitochondrial Dysfunction as a Key to Understanding and Treating Alzheimer's Disease," *Molecular Neurobiology* 57 (2020): 5103–5120.

9. J. Z. Wang, I. Grundke-Iqbal, and K. Iqbal, "Kinases and Phosphatases and Tau Sites Involved in Alzheimer Neurofibrillary Degeneration," *European Journal of Neuroscience* 25 (2007): 59–68.

10. H. Braak, I. Alafuzoff, T. Arzberger, H. Kretzschmar, and K. Del Tredici, "Staging of Alzheimer Disease-Associated Neurofibrillary Pathology Using Paraffin Sections and Immunocytochemistry," *Acta Neuropathologica* 112 (2006): 389–404.

11. R. B. Maccioni, L. E. Rojo, J. A. Fernandez, and R. O. Kuljis, "The Role of Neuroimmunomodulation in Alzheimer's Disease," *Annals of the New York Academy of Sciences* 1153 (2009): 240–246.

12. F. Leng and P. Edison, "Neuroinflammation and Microglial Activation in Alzheimer Disease: Where Do We Go From Here?," *Nature Reviews Neurology* 17 (2021): 157–172.

13. M. L. Block, "NADPH Oxidase as a Therapeutic Target in Alzheimer's Disease," *BMC Neuroscience [Electronic Resource]* 9 (2008): S8.

14. E. Luengo, P. Trigo-Alonso, C. Fernandez-Mendivil, et al., "Implication of Type 4 NADPH Oxidase (NOX4) in Tauopathy," *Redox Biology* 49 (2022): 102210.

15. G. M. Burslem, B. E. Smith, A. C. Lai, et al., "The Advantages of Targeted Protein Degradation Over Inhibition: An RTK Case Study," *Cell Chemical Biology* 25 (2018): 67–77.e3.

16. S. M. Banik, K. Pedram, S. Wisnovsky, G. Ahn, N. M. Riley, and C. R. Bertozzi, "Lysosome-Targeting Chimaeras for Degradation of Extracellular Proteins," *Nature* 584 (2020): 291–297.

17. M. Bekes, D. R. Langley, and C. M. Crews, "PROTAC Targeted Protein Degraders: The Past is Prologue," *Nature reviews Drug discovery* 21 (2022): 181–200, https://doi.org/10.1038/s41573-021-00371-6.

18. Y. H. Jin, M. C. Lu, Y. Wang, et al., "Azo-PROTAC: Novel Light-Controlled Small-Molecule Tool for Protein Knockdown," *Journal of Medicinal Chemistry* 63 (2020): 4644–4654.

19. J. Liu, H. Chen, Y. Liu, et al., "Cancer Selective Target Degradation by Folate-Caged PROTACs," *Journal of the American Chemical Society* 143 (2021): 7380–7387.

20. S. Imaide, K. M. Riching, N. Makukhin, et al., "Trivalent PROTACs Enhance Protein Degradation via Combined Avidity and Cooperativity," *Nature Chemical Biology* 17 (2021): 1157–1167.

21. Y. Wang, L. Han, F. Liu, et al., "Targeted Degradation of Anaplastic Lymphoma Kinase by Gold Nanoparticle-Based Multi-Headed Proteolysis Targeting Chimeras," *Colloids and Surfaces B: Biointerfaces* 188 (2020): 110795.

22. S. Tomoshige and M. Ishikawa, "PROTACs and Other Chemical Protein Degradation Technologies for the Treatment of Neurodegenerative Disorders," *Angewandte Chemie International Edition* 60 (2021): 3346–3354.

23. S. Hyun and D. Shin, "Chemical-Mediated Targeted Protein Degradation in Neurodegenerative Diseases," *Life* 11 (2021): 607.

24. R. B. Kargbo, "Treatment of Alzheimer's by PROTAC-Tau Protein Degradation," *ACS Medicinal Chemistry Letters* 10 (2019): 699–700.

25. X. Liao, G. Qin, Z. Liu, J. Ren, and X. Qu, "Bioorthogonal Aptamer-ATTEC Conjugates for Degradation of Alpha-Synuclein via Autophagy-Lysosomal Pathway," *Small* 20 (2024): 2306760.

26. J. Byun, D. Kim, J. Choi, G. Shim, and Y. K. Oh, "Photosensitizer-Trapped Gold Nanocluster for Dual Light-Responsive Phototherapy," *Biomedicines* 8 (2020): 521.

27. L. Y. Chen, C. W. Wang, Z. Yuan, and H. T. Chang, "Fluorescent Gold Nanoclusters: Recent Advances in Sensing and Imaging," *Analytical Chemistry* 87 (2015): 216–229.

28. D. M. Chevrier, M. A. Macdonald, A. Chatt, P. Zhang, Z. Wu, and R. Jin, "Sensitivity of Structural and Electronic Properties of Gold–Thiolate Nanoclusters to the Atomic Composition: A Comparative X-Ray Study of $Au_{19}(SR)_{13}$ and $Au_{25}(SR)_{18}$," *The Journal of Physical Chemistry C* 116 (2012): 25137–25142.

29. I. Russier-Antoine, F. Bertorelle, M. Vojkovic, et al., "Non-Linear Optical Properties of Gold Quantum Clusters. The Smaller the Better," *Nanoscale* 6 (2014): 13572–13578.

30. G. Salassa, A. Sels, F. Mancin, and T. Burgi, "Dynamic Nature of Thiolate Monolayer in $Au_{25}(SR)_{18}$ Nanoclusters," *ACS Nano* 11 (2017): 12609–12614.

31. J. Jung, S. Kang, and Y. K. Han, "Ligand Effects on the Stability of Thiol-Stabilized Gold Nanoclusters: $Au_{25}(SR)_{18-}$, $Au_{38}(SR)_{24}$, and $Au_{102}(SR)_{44}$," *Nanoscale* 4 (2012): 4206.

32. E. R. Gran, F. Bertorelle, H. Fakhouri, et al., "Size and Ligand Effects of Gold Nanoclusters in Alteration of Organellar State and Translocation of Transcription Factors in Human Primary Astrocytes," *Nanoscale* 13 (2021): 3173–3183.

33. C. N. Loynachan, A. P. Soleimany, J. S. Dudani, et al., "Renal Clearable Catalytic Gold Nanoclusters for In Vivo Disease Monitoring," *Nature Nanotechnology* 14 (2019): 883–890.

34. M. F. Matus and H. Hakkinen, "Atomically Precise Gold Nanoclusters: Towards an Optimal Biocompatible System from a Theoretical–Experimental Strategy," *Small* 17 (2021): 2005499.

35. C. Peng, X. Gao, J. Xu, et al., "Targeting Orthotopic Gliomas With Renal-Clearable Luminescent Gold Nanoparticles," *Nano Research* 10 (2017): 1366–1376.

36. E. Porret, X. L. Guevel, and J. L. Coll, "Gold Nanoclusters for Biomedical Applications: Toward In Vivo Studies," *Journal of Materials Chemistry B* 8 (2020): 2216–2232.

37. H. Khan, T. G. Singh, R. S. Dahiya, and M. M. Abdel-Daim, "α-Lipoic Acid, an Organosulfur Biomolecule a Novel Therapeutic Agent for Neurodegenerative Disorders: An Mechanistic Perspective," *Neurochemical Research* 47 (2022): 1853–1864, https://doi.org/10.1007/s11064-022-03598-w.

38. L. Xiao, F. Wei, Y. Zhou, et al., "Dihydrolipoic Acid–Gold Nanoclusters Regulate Microglial Polarization and Have the Potential to Alter Neurogenesis," *Nano Letters* 20 (2020): 478–495.

39. D. Mishra, F. Aldeek, E. Lochner, et al., "Aqueous Growth of Gold Clusters With Tunable Fluorescence Using Photochemically Modified Lipoic Acid-Based Ligands," *Langmuir* 32 (2016): 6445–6458.

40. A. Shahid, K. Nasir, and M. Bhatia, "Therapeutic Potential of Alpha-Lipoic Acid: Unraveling Its Role in Oxidative Stress and Inflammatory Conditions," *Current Issues in Molecular Biology* 47 (2025): 322.

41. A. Maczurek, K. Hager, M. Kenklies, et al., "Lipoic Acid as an Anti-Inflammatory and Neuroprotective Treatment for Alzheimer's Disease," *Advanced Drug Delivery Reviews* 60 (2008): 1463–1470.

42. J. Zhang, M. Wang, Y. Zhao, et al., "Alpha-Lipoic Acid Improved Motor Function in MPTP-Induced Parkinsonian Mice by Reducing

Neuroinflammation in the Nigral and Spinal Cord," *Neuroscience Letters* 781 (2022): 136669.

43. K. Zhou, B. Enkhjargal, Z. Xie, et al., "Dihydrolipoic Acid Inhibits Lysosomal Rupture and NLRP3 Through Lysosome-Associated Membrane Protein-1/Calcium/Calmodulin-Dependent Protein Kinase II/TAK1 Pathways After Subarachnoid Hemorrhage in Rat," *Stroke; A Journal of Cerebral Circulation* 49 (2018): 175–183.

44. M. Akbari, V. Ostadmohammadi, R. Tabrizi, et al., "The Effects of Alpha-Lipoic Acid Supplementation on Inflammatory Markers Among Patients With Metabolic Syndrome and Related Disorders: A Systematic Review and Meta-Analysis of Randomized Controlled Trials," *Nutrition & Metabolism* 15 (2018): 39.

45. D. W. Li, Y. D. Wang, S. Y. Zhou, and W. P. Sun, "α-Lipoic Acid Exerts Neuroprotective Effects on Neuronal Cells by Upregulating the Expression of PCNA via the P53 Pathway in Neurodegenerative Conditions," *Molecular Medicine Reports* 14 (2016): 4360–4366.

46. L. Lai, C. Zhao, X. Li, et al., "Fluorescent Gold Nanoclusters for In Vivo Target Imaging of Alzheimer's Disease," *RSC Advances* 6 (2016): 30081–30088.

47. Y. W. Lai, Y. N. Lee, H. I. Yeh, et al., "Long-Term Safety Evaluation of Fluorescent Gold Nanoclusters Conjugated With α-Lipoic Acid: Insights from a Six-Month In Vivo Study," *Journal of Functional Biomaterials* 16 (2025): 89.

48. Y. F. Chen, C. C. Hsu, and C. H. Chung, "Acute and Subacute Toxicity of Fluorescent Gold Nanoclusters Conjugated With α-Lipoic Acid," *Nanomaterials* 12 (2022): 3868.

49. K. Susumu, B. C. Mei, and H. Mattoussi, "Multifunctional Ligands Based on Dihydrolipoic Acid and Polyethylene Glycol to Promote Biocompatibility of Quantum Dots," *Nature Protocols* 4 (2009): 424–436.

50. S. Onder, K. Biberoglu, M. Yuksel, and O. Tacal, "Toluidine Blue O Attenuates Tau Phosphorylation in N2a-APPSwe Cells," *Chemico-Biological Interactions* 366 (2022): 110126.

51. M. Yuksel, K. Biberoglu, S. Onder, K. G. Akbulut, and O. Tacal, "Toluidine Blue O Modifies Hippocampal Amyloid Pathology in a Transgenic Mouse Model of Alzheimer's Disease," *Biochimie* 146 (2018): 105–112.

52. T. Dubey, N. V. Gorantla, K. T. Chandrashekara, and S. Chinnathambi, "Photoexcited Toluidine Blue Inhibits Tau Aggregation in Alzheimer's Disease," *ACS Omega* 4 (2019): 18793–18802.

53. E. R. Watson, S. Novick, M. E. Matyskiela, et al., "Molecular Glue CELMoD Compounds are Regulators of Cereblon Conformation," *Science* 378 (2022): 549–553.

54. M. Girardini, C. Maniaci, S. J. Hughes, A. Testa, and A. Ciulli, "Cereblon Versus VHL: Hijacking E3 Ligases Against Each Other Using PROTACs," *Bioorganic & Medicinal Chemistry* 27 (2019): 2466–2479.

55. F. Aldeek, M. A. H. Muhammed, G. Palui, N. Zhan, and H. Mattoussi, "Growth of Highly Fluorescent Polyethylene Glycol- and Zwitterion-Functionalized Gold Nanoclusters," *ACS Nano* 7 (2013): 2509–2521.

56. K. Cyrus, M. Wehenkel, E. Y. Choi, et al., "Impact of Linker Length on the Activity of PROTACs," *Molecular BioSystems* 7 (2011): 359–364.

57. L. Luo, Z. Liu, X. Du, and R. Jin, "Photoluminescence of the $Au_{38}(SR)_{26}$ Nanocluster Comprises Three Radiative Processes," *Communications Chemistry* 6 (2023): 22.

58. Y. Li, Y. Song, X. Zhang, et al., "Atomically Precise Au_{42} Nanorods With Longitudinal Excitons for an Intense Photothermal Effect," *Journal of the American Chemical Society* 144 (2022): 12381–12389.

59. C. Zeng, Y. Chen, C. Liu, K. Nobusada, N. L. Rosi, and R. Jin, "Gold Tetrahedra Coil Up: Kekulé-Like and Double Helical Superstructures," *Science Advances* 1 (2015): 1500425.

60. M. Boban, M. Babic Leko, T. Miskic, P. R. Hof, and G. Simic, "Human Neuroblastoma SH-SY5Y Cells Treated With Okadaic Acid Express Phosphorylated High Molecular Weight Tau-Immunoreactive Protein Species," *Journal of Neuroscience Methods* 319 (2019): 60–68.

61. Z. Chen, B. Chen, W. F. Xu, R. F. Liu, J. Yang, and C. X. Yu, "Effects of PTEN Inhibition on Regulation of Tau Phosphorylation in an Okadaic Acid-Induced Neurodegeneration Model," *International Journal of Developmental Neuroscience* 30 (2012): 411–419.

62. A. Bretteville, F. Marcouiller, C. Julien, et al., "Hypothermia-Induced Hyperphosphorylation: A New Model to Study Tau Kinase Inhibitors," *Scientific Reports* 2 (2012): 480.

63. P. K. Kamat, S. Rai, and C. Nath, "Okadaic Acid Induced Neurotoxicity: An Emerging Tool to Study Alzheimer's Disease Pathology," *Neurotoxicology* 37 (2013): 163–172.

64. P. K. Kamat, S. Rai, S. Swarnkar, et al., "Okadaic Acid-Induced Tau Phosphorylation in Rat Brain: Role of NMDA Receptor," *Neuroscience* 238 (2013): 97–113.

65. D. Metin-Armagan, D. Gezen-Ak, E. Dursun, et al., "Okadaic Acid–Induced Tau Hyperphosphorylation and the Downregulation of Pin1 Expression in Primary Cortical Neurons," *Journal of Chemical Neuroanatomy* 92 (2018): 41–47.

66. H. Zhang, X. Wang, P. Xu, et al., "Tolfenamic Acid Inhibits GSK-3β and PP2A Mediated Tau Hyperphosphorylation in Alzheimer's Disease Models," *The Journal of Physiological Sciences* 70 (2020): 29.

67. Z. Zhang and J. W. Simpkins, "Okadaic Acid Induces Tau Phosphorylation in SH-SY5Y Cells in an Estrogen-Preventable Manner," *Brain Research* 1345 (2010): 176–181.

68. G. Lepski, J. Maciaczyk, C. E. Jannes, D. Maciaczyk, J. Bischofberger, and G. Nikkhah, "Delayed Functional Maturation of Human Neuronal Progenitor Cells In Vitro," *Molecular and Cellular Neuroscience* 47 (2011): 36–44.

69. E. N. Benveniste, V. T. Nguyen, and D. R. Wesemann, "Molecular Regulation of CD40 Gene Expression in Macrophages and Microglia," *Brain, Behavior, and Immunity* 18 (2004): 7–12.

70. P. Buchhave, S. Janciauskiene, H. Zetterberg, K. Blennow, L. Minthon, and O. Hansson, "Elevated Plasma Levels of Soluble CD40 in Incipient Alzheimer's Disease," *Neuroscience Letters* 450 (2009): 56–59.

71. A. D. Greenhalgh, S. David, and F. C. Bennett, "Immune Cell Regulation of Glia During CNS Injury and Disease," *Nature Reviews Neuroscience* 21 (2020): 139–152.

72. R. T. Han, R. D. Kim, A. V. Molofsky, and S. A. Liddelow, "Astrocyte-Immune Cell Interactions in Physiology and Pathology," *Immunity* 54 (2021): 211–224.

73. S. A. Liddelow, S. E. Marsh, and B. Stevens, "Microglia and Astrocytes in Disease: Dynamic Duo or Partners in Crime?," *Trends in Immunology* 41 (2020): 820–835.

74. Z. Tang, Z. Chen, M. Guo, et al., "NRF2 Deficiency Promotes Ferroptosis of Astrocytes Mediated by Oxidative Stress in Alzheimer's Disease," *Molecular Neurobiology* 61 (2024): 7517–7533, https://doi.org/10.1007/s12035-024-04023-9.

75. M. G. Elhadidy, A. Elmasry, H. R. H. Elsayed, et al., "Modulation of COX-2 and NADPH Oxidase-4 by Alpha-Lipoic Acid Ameliorates Busulfan-Induced Pulmonary Injury in Rats," *Heliyon* 7 (2021): 08171.

76. D. Kaur, T. Behl, A. Sehgal, et al., "RETRACTED: Decrypting the Potential Role of α-Lipoic Acid in Alzheimer's Disease," *Life Sciences* 284 (2021): 119899.

77. H. Herd, N. Daum, A. T. Jones, H. Huwer, H. Ghandehari, and C. M. Lehr, "Nanoparticle Geometry and Surface Orientation Influence Mode of Cellular Uptake," *ACS Nano* 7 (2013): 1961–1973.

78. M. D. Sweeney, Z. Zhao, A. Montagne, A. R. Nelson, and B. V. Zlokovic, "Blood-Brain Barrier: From Physiology to Disease and Back," *Physiological Reviews* 99 (2019): 21–78.

79. E. G. Knox, M. R. Aburto, G. Clarke, J. F. Cryan, and C. M. O'Driscoll, "The Blood-Brain Barrier in Aging and Neurodegeneration," *Molecular Psychiatry* 27 (2022): 2659–2673.

80. P. R. Clark, T. D. Manes, J. S. Pober, and M. S. Kluger, "Increased ICAM-1 Expression Causes Endothelial Cell Leakiness, Cytoskeletal Reorganization and Junctional Alterations," *Journal of Investigative Dermatology* 127 (2007): 762–774.

81. E. A. Winkler, Y. Nishida, A. P. Sagare, et al., "GLUT1 Reductions Exacerbate Alzheimer's Disease Vasculo-Neuronal Dysfunction and Degeneration," *Nature Neuroscience* 18 (2015): 521–530.

82. D. Otgongerel, H. J. Lee, and S. A. Jo, "Induction of ICAM1 in Brain Vessels is Implicated in an Early AD Pathogenesis by Modulating Neprilysin," *NeuroMolecular Medicine* 25 (2023): 193–204.

83. J. Xue, P. B. Thippegowda, G. Hu, et al., "NF-κB Regulates Thrombin-Induced ICAM-1 Gene Expression in Cooperation With NFAT by Binding to the Intronic NF-κB Site in the ICAM-1 Gene," *Physiological Genomics* 38 (2009): 42–53.

84. D. C. Hess, T. Bhutwala, J. C. Sheppard, W. Zhao, and J. Smith, "ICAM-1 Expression on Human Brain Microvascular Endothelial Cells," *Neuroscience Letters* 168 (1994): 201–204.

85. S. K. Solders, Q. Shen, and E. T. Reas, "Blood-Brain Barrier Permeability Varies by Brain Region and APOE4 Status and Correlates With Brain Microstructure Among High-AD Risk Groups," *NeuroImage: Clinical* 46 (2025): 103805.

86. X. D. Zhang, D. Wu, X. Shen, P. X. Liu, F. Y. Fan, and S. J. Fan, "In Vivo Renal Clearance, Biodistribution, Toxicity of Gold Nanoclusters," *Biomaterials* 33 (2012): 4628–4638.

87. F. St-Onge, M. Chapleau, J. C. S. Breitner, S. Villeneuve, and A. P. Binette, "Tau Accumulation and Its Spatial Progression Across the Alzheimer's Disease Spectrum," *Brain Communications* 6 (2024): fcae031.

88. M. J. Reid, P. Beltran-Lobo, L. Johnson, B. G. Perez-Nievas, and W. Noble, "Astrocytes in Tauopathies," *Frontiers in Neurology* 11 (2020): 572850.

Supporting Information

Additional supporting information can be found online in the Supporting Information section.

Supporting File: adfm76374-sup-0001-SuppMat.docx.